*J. Fluid Mech.* (2014), *vol.* 758, *pp.* 728–753.  
doi:10.1017/jfm.2014.553

# A dynamic observer to capture and control perturbation energy in noise amplifiers

**Juan Guzmán Iñigo[1],†, Denis Sipp[1] and Peter J. Schmid[2]**

[1]Département d'Aérodynamique Fondamentale et Expérimentale, ONERA, 8 Rue des Vertugadins, 92190 Meudon, France

[2]Department of Mathematics, Imperial College London, South Kensington Campus, London SW7 2AZ, UK

(Received 21 January 2014; revised 4 September 2014; accepted 18 September 2014)

In this article, we introduce techniques to build a reduced-order model of a fluid system that accurately predicts the dynamics of a flow from local wall measurements. This is particularly difficult in the case of noise amplifiers where the upstream noise environment, triggering the flow via a receptivity process, is not known. A system identification approach, rather than a classical Galerkin technique, is used to extract the model from time-synchronous velocity snapshots and wall shear-stress measurements. The technique will be illustrated for the case of a transitional flat-plate boundary layer, where the snapshots of the flow are obtained from direct numerical simulations. Particular attention is directed to limiting the processed data to data that would be readily available in experiments, thus making the technique applicable to an experimental set-up. The proposed approach combines a reduction of the degrees of freedom of the system by a projection of the velocity snapshots onto a proper orthogonal decomposition basis combined with a system identification technique to obtain a state-space model. This model is then used in a feedforward control set-up to significantly reduce the kinetic energy of the perturbation field and thus successfully delay transition.

**Key words:** boundary layer control, control theory, instability control

## 1. Introduction

Fluid systems that fall under the category of noise amplifiers are characterized by a globally stable spectrum despite the presence of convective instabilities. Boundary layers are examples of this type of fluid behaviour. External perturbations permeate the near-wall region during the receptivity phase and initiate disturbances that are amplified into Tollmien–Schlichting waves as they are swept downstream. If these instabilities reach sufficient amplitudes, breakdown of the flow into turbulent fluid motion can occur. Much effort has been expended to understand and control this breakdown into turbulence by manipulating the underlying instability processes.

While many open-loop control techniques have been developed to delay the transition process, closed-loop approaches, where actuation depends on sensor

† Email address for correspondence: juan.guzman.inigo@gmail.com

measurements, are more effective and efficient (Kim & Bewley 2007). However, under realistic flow conditions, the direct application of closed-loop control techniques is often not tractable. The high degrees of freedom of fluid systems (often $O(10^6)$) are far beyond the capabilities of current control devices, which typically can handle $O(10^2)$ variables. As a consequence, the full fluid system has to be properly reduced, before a controller can be designed for the reduced-order model (ROM). This methodology has been demonstrated to yield successful control designs (see Bagheri, Brandt & Henningson 2009; Barbagallo, Sipp & Schmid 2009, among others). In these investigations, model reduction is accomplished by a flow decomposition (e.g. proper orthogonal decomposition (POD) or balanced proper orthogonal decomposition (BPOD)) followed by a Galerkin projection of the equations onto the reduced basis.

In the case of noise amplifiers, external perturbations strongly influence the system dynamics. Thus, it is very important for the ROM to accurately capture the noise environment. In particular, ROMs obtained by means of Galerkin projections require detailed knowledge of the spatial distribution of the upstream noise sources. This requirement imposes great limitations, especially in experimental situations, where information about the noise environment is neither directly nor sufficiently available. A promising alternative to control design based on Galerkin projections derives from system identification techniques as proposed in Hervé *et al.* (2012); this approach also constitutes an encouraging step towards the control of noise amplifiers in experimental situations.

This paper intends to provide a methodology to obtain reduced-order estimators for noise amplifiers without using Galerkin projections. While in Hervé *et al.* (2012) the model describes only the dynamics between one sensor (upstream measurement) and another (downstream measurement), here we aim to capture the dynamics between upstream measurements and the entire perturbation field. This will allow the reconstruction of the full flow field and, consequently, the design of controllers that target the kinetic energy of the full perturbation field, not only the variance of a wall measurement signal. This brings to mind the Galerkin-based output projection technique introduced by Rowley (2005), which captures the full perturbation field from a given input. However, the latter technique requires precise knowledge of the spatial distribution of the input, which is generally not available in amplifier flows. Therefore, Dergham, Sipp & Robinet (2013) have extended it to account also for any possible input, so as to obtain a model that captures any input to any output. In the present work, we aim to obtain a similar model – capturing the dynamics from unknown input to any output – but with identification methods. The proposed approach consists of a reduction of the degrees of freedom of the system by (i) a projection of the velocity fields onto a reduced basis combined with (ii) a system identification algorithm to obtain the dynamic operators of a reduced-order system. In particular, a link between velocity fields (e.g. from time-resolved particle image velocimetry (TR-PIV) data) and time-synchronous wall shear-stress measurements is established, and a dynamic observer is determined. A key feature of our procedure is its reliance on a Galerkin model structure, but on the determination of the model matrices by system identification rather than by integral expressions (Galerkin projections).

The link between velocity fields and wall measurements is reminiscent of linear stochastic estimation (LSE) techniques (Adrian 1979; Guezennec 1989; Bonnet *et al.* 1994; Taylor & Glauser 2004; Tinney *et al.* 2006; Hudy, Naguib & Humphreys 2007; Tu *et al.* 2013), where multiple measured inputs are correlated to simultaneous multiple outputs by averaging over many realizations. Our proposed technique generalizes this static approach by accounting for the dynamics of either measurement

data. The comparison between LSE and dynamic observers obtained by Galerkin projection has already been considered in Rowley & Juttijudata (2005), showing the superiority of dynamic estimators. A further relation can be demonstrated to data assimilation techniques, specifically, to the online variant (see e.g. Lewis, Lakshmivarahan & Dhall 1989) where streaming data are matched to an underlying model, which is then used to predict future measurement signals. Once a model has been extracted by our technique from measured data, it can straightforwardly be used in a closed-loop control application, as will be illustrated below.

The present study is structured as follows. After a brief description of the flow configuration and the governing equations (§ 2), we present a dynamic observer obtained by Galerkin projection (§ 3) and by the identification procedure (§ 4). Section 5 will compare the identified observer with different well-known approaches, while § 6 will demonstrate how to include the identified model in a control framework. A summary of results and conclusions are given in § 7. Appendix A gives details about the employed subspace system identification techniques.

## 2. Problem formulation

### 2.1. *Governing equations*

We choose a zero-pressure gradient boundary layer – a classical and generic flow that acts as a noise amplifier – as our configuration to design and test the dynamic observer. This flow is globally stable but selectively amplifies upstream disturbances by convective instabilities. In a low-amplitude noise environment, two-dimensional Tollmien–Schlichting waves appear as a result of this instability mechanism.

We consider the dynamics of disturbances $\boldsymbol{u}$ around a base flow $\boldsymbol{U}_0$, which we take as a Blasius boundary layer. The disturbances $\boldsymbol{u}$ are additionally driven by an external forcing term, $\boldsymbol{F}_w w(t)$, which acts as an upstream disturbance source of unknown origin. For simplicity, we assume that $w(t)$ is a random process of zero mean and variance $W$, while $\boldsymbol{F}_w$ describes a spatial two-dimensional Gaussian distribution centred at $(x_w, y_w)$ of spread $(\sigma_x, \sigma_y)$ and amplitude $A$. The spatio-temporal evolution of the total flow field, $\boldsymbol{U}_{tot} = \boldsymbol{U}_0 + \boldsymbol{u}$, is governed by the incompressible Navier–Stokes equations, augmented by a forcing term,

$$\partial_t \boldsymbol{U}_{tot} + \boldsymbol{U}_{tot} \cdot \boldsymbol{\nabla} \boldsymbol{U}_{tot} = -\boldsymbol{\nabla} P_{tot} + Re_{\delta_0^*}^{-1} \Delta \boldsymbol{U}_{tot} + \boldsymbol{F}_w w(t), \quad \boldsymbol{\nabla} \cdot \boldsymbol{U}_{tot} = 0. \tag{2.1a,b}$$

The variables are non-dimensionalized using the displacement thickness $\delta_0^*$ of the boundary layer at the computational inlet ($x_0 = 0$) and the free-stream velocity $U_\infty$. Consequently, the Reynolds number is defined as $Re_{\delta_0^*} = U_\infty \delta_0^* / \nu$. All simulations were performed at $Re_{\delta_0^*} = 1000$, which ensures the presence of strong Tollmien–Schlichting instabilities, since $Re_{\delta_0^*} > Re_{\delta^*}^{crit} = 520$.

The governing equations (2.1) are solved in a computational domain $\Omega$ of size $(0, 1000) \times (0, 40)$, sketched in figure 1. A Blasius profile of unit displacement thickness is prescribed at the left boundary, outflow conditions are employed at the upper and right boundaries, and a no-slip condition is imposed at the wall. We use the spectral-element code Nek5000 (see https://nek5000.mcs.anl.gov) to perform the computations below.

With the base flow $\boldsymbol{U}_0$ as a solution of the unforced ($w = 0$) steady Navier–Stokes equations (2.1), the perturbations $\boldsymbol{u}$ are governed by the following equations:

$$\partial_t \boldsymbol{u} + \boldsymbol{U}_0 \cdot \boldsymbol{\nabla} \boldsymbol{u} + \boldsymbol{u} \cdot \boldsymbol{\nabla} \boldsymbol{U}_0 = -\boldsymbol{\nabla} p + Re_{\delta_0^*}^{-1} \Delta \boldsymbol{u} + \boldsymbol{F}_w w(t), \quad \boldsymbol{\nabla} \cdot \boldsymbol{u} = 0. \tag{2.2a,b}$$

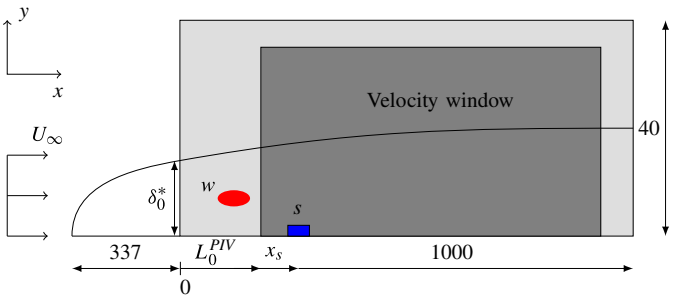


FIGURE 1. (Colour online) Sketch of the flow configuration. The computational domain $\Omega$ is of size $(0, 1000) \times (0, 40)$, represented by the light grey box. The upstream receptivity of the boundary layer to external perturbations is modelled by the noise $w$, which is placed at $(x_w, y_w) = (50, 0.95)$. A sensor located at $(x_s, y_s) = (200, 0)$ will identify incoming perturbations, while a velocity window (represented by the dark grey box) is used to quantify the effect of the forcing on the velocity field.

Here the nonlinear term $\boldsymbol{u} \cdot \nabla \boldsymbol{u}$ has been omitted since only low-amplitude noise $W \ll 1$ will be considered. This assumption ensures linear perturbation dynamics, as well as a linear response to the noise $w$. During the direct numerical simulations (DNS), white noise is imposed via $w(n)$ to mimic upstream excitations of unknown source and distribution (mimicking conditions in physical experiments). We use a time step of $\mathrm{d}t_{DNS} = 0.1$.

### 2.2. *Perturbation dynamics*

Choosing the Blasius boundary layer as an example of a noise amplifier and assuming a low-noise environment, perturbations may be amplified by two different instability mechanisms: (i) the Tollmien–Schlichting instability, which takes advantage of a critical layer as well as a wall layer to generate a non-zero Reynolds stress, and (ii) the Orr instability, where initial perturbations lean against the mean shear but grow in amplitude as they are tilted by the mean velocity (Butler & Farrell 1992). The details of these mechanisms can be studied within a local stability framework, considering perturbations of the form $\mathrm{e}^{\mathrm{i}(\alpha x - \omega t)}$, with $\omega$ the frequency and $\alpha$ the streamwise wavenumber of the perturbation. An analysis of this type shows that the Blasius boundary layer is convectively unstable to Tollmien–Schlichting waves when the Reynolds number based on the local displacement thickness $\delta^*(x)$ is larger than the critical value of $Re = 520$. In figure 2, the neutral curve obtained from a local spatial stability analysis performed with wall-normal profiles extracted from the base flow $\boldsymbol{U}_0$ is displayed. The unstable frequencies fall in the interval $0.055 < \omega < 0.13$ at the computational inlet and $0.015 < \omega < 0.052$ at the end of the domain. When a localized disturbance is placed inside the boundary layer, the response is a wavepacket that convects downstream at the local group velocity $v_g = \mathrm{d}\omega/\mathrm{d}\alpha$. The group velocity is a very important parameter, as it sets a characteristic time for the perturbation, and can easily be obtained from the dispersion relation $\omega = \omega(\alpha)$. In figure 3, the dispersion relation is represented for three different Reynolds numbers (corresponding to streamwise locations at the computational inlet, middle and outlet). For the considered configuration, the group velocity is estimated as $v_g \approx 0.375 U_\infty$ using the real-axis approximation.

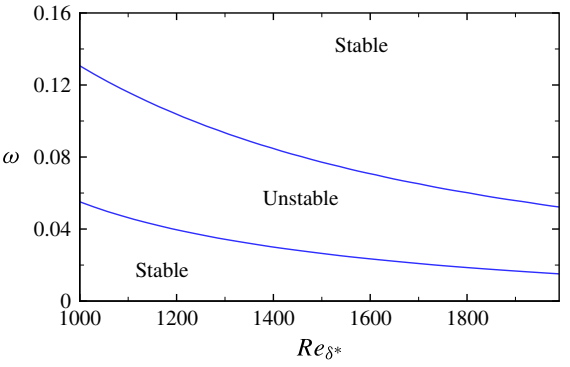


FIGURE 2. (Colour online) Neutral curve obtained by a local spatial stability analysis in the computational domain.

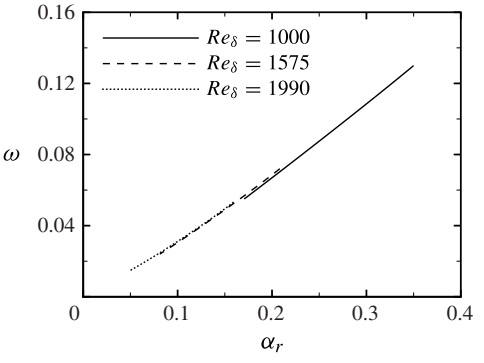


FIGURE 3. Spatial dispersion relation for the convectively unstable frequencies at three different positions within the domain.

### 2.3. *Measurements*

This paper aims to provide a data-based technique that is applicable in an experimental setting. For this reason, special care must be taken to use only data that are readily available in an experiment. We first consider a wall-friction sensor $s$ (see figure 1), located at $x_s = 200$ and of spatial extension in the streamwise direction $\Delta x = 0.5$, which measures the wall shear stress,

$$\begin{aligned} s_{tot} &= \int_{x_s}^{x_s+\Delta x} \left.\frac{\partial u_{tot}}{\partial y}\right|_{y=0} \mathrm{d}x + g \\ &= \int_{x_s}^{x_s+\Delta x} \left.\frac{\partial U_0}{\partial y}\right|_{y=0} \mathrm{d}x + \underbrace{\int_{x_s}^{x_s+\Delta x} \left.\frac{\partial u}{\partial y}\right|_{y=0} \mathrm{d}x + g}_{s(t)}, \end{aligned} \tag{2.3}$$

where $s$ denotes the fluctuating part of the measurement, which may be obtained by subtracting the time-averaged value of $s_{tot}$ from the signal $s_{tot}$. For the case of low-amplitude forcing, i.e. for linear perturbation dynamics, the time-averaged value also corresponds to the base-flow value. The sensor $s_{tot}$ (or $s$) may be corrupted by white noise $g$, of variance $G$ (with $G$ small and of the order of magnitude of $W$).

In addition to the wall-friction sensor $s$, we also consider velocity snapshots $\boldsymbol{u}_{snap}$ in a given domain $\Omega_{snap}$, which may be chosen smaller than the computational domain $\Omega$ (see figure 1). The fluctuating parts of the velocity field may again be obtained by subtracting the time-averaged snapshots from the total snapshot sequence. In an experimental set-up, the velocity snapshots may be obtained by a PIV technique. In what follows, we will consider time series of composite skin-friction measurements and velocity snapshots.

## 3. Structure of a dynamic observer using Galerkin projection

In this section the model reduction technique based on Galerkin projection will be briefly discussed to motivate the use of identification methods in the design of ROMs. Special attention will be paid to the structure of the resulting model since it will form the basis of the system identification approach. We proceed by developing and analysing the ROM that would result from a projection of the linearized Navier–Stokes equations onto a POD basis (§ 3.1), which is followed by the introduction of a Kalman filter allowing us to replace the unknown driving term $w(t)$ by the known measurements $s(t)$ (§ 3.2).

### 3.1. *Reduced-order model with Galerkin projection by approximation of the controllability Gramian*

A common method used to obtain a ROM of a dynamical system is based on Galerkin projection, i.e. a projection of the Navier–Stokes equations (2.2) onto an appropriate basis, such that the input–output behaviour of the full system is preserved as accurately as possible. The choice of basis is critical. The two most common options are based on: an approximation of the controllability Gramian, which yields a POD basis (Rowley 2005; Barbagallo *et al.* 2009) that maximizes the energy captured by the ROM, and an approximation of the controllability and observability Gramians, which yields a balanced basis (Moore 1981; Rowley 2005; Bagheri *et al.* 2009) that directly focuses on the input–output relation of the reduced system. In this article, only ROMs obtained by approximating the controllability Gramian will be considered.

After extracting the POD modes (taking data from the full computational domain) from the approximation of the controllability Gramian by an impulse response of the full system (see Barbagallo *et al.* 2009 for details), the governing equations (2.2) are projected onto the first $k$ modes to obtain a reduced state-space representation of the system according to

$$\frac{\mathrm{d}\boldsymbol{X}}{\mathrm{d}t} = \boldsymbol{A}'_w \boldsymbol{X}(t) + \boldsymbol{B}'_w w(t), \tag{3.1a}$$

$$s(t) = \boldsymbol{C}' \boldsymbol{X}(t) + g(t), \tag{3.1b}$$

where $\boldsymbol{X}(t)$ is a vector containing the $k$ POD coefficients at time $t$. Denoting by $\langle\cdot\rangle$ the energy-based inner product that has been used to extract the POD modes, the components of the matrix $\boldsymbol{A}'_w$ and of the vectors $\boldsymbol{B}'_w$ and $\boldsymbol{C}'$ are obtained as follows: $A'_{w,ij} = \langle \boldsymbol{\Phi}_i, \mathscr{A}\boldsymbol{\Phi}_j \rangle$ (with $\mathscr{A}$ the linearized Navier–Stokes operator (2.2) on $\Omega$), $B'_{w,i} = \langle \boldsymbol{\Phi}_i, \boldsymbol{F}_w \rangle$ and $C'_i = \mathscr{C}\boldsymbol{\Phi}_i$ (with $\mathscr{C}$ as the measurement operator).

A Galerkin projection usually provides a continuous-time format for the state-space system (3.1). With the remainder of the article pertaining to system identification methods, it is more convenient to express the governing equations in a discrete-time

framework. In the discrete-time domain, the mapping of the state vector $\boldsymbol{X}$ from time $t$ (index $n$) to $t+\Delta t$ (index $n+1$) reads

$$\boldsymbol{X}(n+1) = \boldsymbol{A}_w \boldsymbol{X}(n) + \boldsymbol{B}_w w(n), \tag{3.2a}$$

$$s(n) = \boldsymbol{C}\boldsymbol{X}(n) + g(n), \tag{3.2b}$$

with $\boldsymbol{B}_w = \int_0^{\Delta t} \exp[\boldsymbol{A}_w'(\Delta t - \tau)]\boldsymbol{B}_w' \mathrm{d}\tau$ associated with the discrete driving term, $\boldsymbol{A}_w = \exp(\boldsymbol{A}_w' \Delta t)$ denoting the evolution matrix over a time interval $\Delta t$ and $\boldsymbol{C} = \boldsymbol{C}'$.

### 3.2. *Kalman filter*

When dealing with noise amplifiers, it is critical to accurately account for the disturbance environment, as it both triggers and sustains the dynamics of the system. Despite this requirement, in an experimental set-up, access to accurate information about the noise environment is, at best, very difficult or, in most cases, impossible. We thus have to introduce an observer where the noise source term $\boldsymbol{B}_w w(t)$ is replaced by a measurement term $\boldsymbol{L}s(t)$ that drives, as best as possible, the estimated state of the system. Formally, the observer may be obtained in a straightforward manner by introducing a linear estimator of the form

$$\boldsymbol{X}_e(n+1) = \boldsymbol{A}_w \boldsymbol{X}_e(n) + \boldsymbol{L}[s(n) - \boldsymbol{C}\boldsymbol{X}_e(n)] = \boldsymbol{A}_s \boldsymbol{X}_e(n) + \boldsymbol{L}s(n), \tag{3.3}$$

where $\boldsymbol{X}_e(n)$ is the estimated state, $s(n)$ is the measurement signal from the friction sensor (defined by (2.3)) and $\boldsymbol{L}$ represents the gain of the estimator, which can be selected by the designer to achieve different objectives. If the gain $\boldsymbol{L}$ is selected to statistically minimize the error $\|\boldsymbol{X}_e - \boldsymbol{X}\|_2$, the estimator is referred to as a Kalman filter and $\boldsymbol{L}$ is obtained by solving a Riccati equation (see Burl 1999) of the form

$$\boldsymbol{P} = \boldsymbol{A}_w \boldsymbol{P} \boldsymbol{A}_w^* - \boldsymbol{A}_w \boldsymbol{P} \boldsymbol{C}^* (\boldsymbol{C}\boldsymbol{P}\boldsymbol{C}^* + G)^{-1} \boldsymbol{C}\boldsymbol{P}\boldsymbol{A}_w^* + \boldsymbol{B}_w W \boldsymbol{B}_w^*, \tag{3.4a}$$

$$\boldsymbol{L} = \boldsymbol{A}_w \boldsymbol{P} \boldsymbol{C}^* (\boldsymbol{C}\boldsymbol{P}\boldsymbol{C}^* + G)^{-1}. \tag{3.4b}$$

In short, the dynamic observer (3.3) consists of a linear relationship between two subsequent state vectors $\boldsymbol{X}_e(n+1)$ and $\boldsymbol{X}_e(n)$ and the measurement $s(n)$. Its dynamics is fully determined by the evolution matrix $\boldsymbol{A}_s = \boldsymbol{A}_w - \boldsymbol{L}\boldsymbol{C}$ and the observer gain $\boldsymbol{L}$. We stress that this estimator is effective only if the measurement $s$ remains constant over the sampling time $\Delta t$; for this reason, a spectral analysis of the measurement $s$ must be employed to determine its frequency content and thus the sampling time $\Delta t$.

### 3.3. *Limitations of Galerkin-based methods*

Galerkin models based on Gramians are a popular choice for model reduction, owing to their ease of use in feedback applications, the availability of mathematical bounds on their convergence and their link to physically relevant flow structures. But despite their widespread use, Galerkin-based methods for the computation of ROMs suffer from notable limitations when they are applied to experimental situations.

The favourable properties of the Galerkin model presented in this section stem from the fact that the POD modes were obtained by accurately discretizing the integral involved in the controllability Gramian. This requires that an impulse of $w(t)$ can be generated and its response can be analysed using velocity snapshots. Furthermore, a very small delay between two successive snapshots and a very long series of snapshots is desirable. If such requirements are not met, Galerkin projection

then provides POD-based models that may even become unstable: *a posteriori* regularization and calibration techniques are then required to render the models stable again (Bergmann, Bruneau & Iollo 2009).

One of the most important limitations of Galerkin-based models is linked to the requirement for a very accurate distribution of the noise sources in the experiment for amplifier flows, since these sources will drive the dynamics of the system. Generally, the noise distribution in experimental set-ups will be complex, difficult to represent and mostly unknown, so that triggering by an impulse in $w(t)$ is nearly impossible.

## 4. Dynamic observer using system identification techniques

This section introduces an alternative method to obtain a dynamic observer. We will present a data-driven approach, based on system identification techniques, that relies solely on observations of the system in the presence of unknown upstream noise $w(t)$. System identification techniques represent a family of algorithms that efficiently determine the coefficients of an underlying model directly from observed input–output data via a statistical learning process. This section aims to obtain a dynamic observer model such as (3.3) directly from observations of the system. In the following, we will first briefly recall the basics of system identification techniques, which generate a model governing the dynamics of given outputs from known inputs (§ 4.1). Second, we will define the output of our system as the coefficients of the velocity snapshots in a POD basis (§ 4.2). Third, we will introduce the model structure of the dynamic observer (§ 4.3), identify the coefficients of the model (§ 4.4) and validate the model (§ 4.5). Finally, the influence of various parameters on the quality of the model will be assessed (§ 4.6).

### 4.1. *System identification based on subspace techniques*

System identification comprises a wide range of methods of varying applicability and complexity (see Ljung 1999). In our case, we aim to obtain a linear time-invariant (LTI) multiple-input–multiple-output (MIMO) system, such as the one given in (3.3). In general, we have $\boldsymbol{u}(n)$ as known inputs, $\boldsymbol{w}(n)$ as unknown white plant noise and $\boldsymbol{y}(n)$ as known outputs corrupted by unknown white noise $\boldsymbol{v}(n)$. We aim to determine the system matrices ($\boldsymbol{\mathcal{A}}$, $\boldsymbol{\mathcal{B}}$, $\boldsymbol{\mathcal{C}}$ and $\boldsymbol{\mathcal{D}}$), which govern a state $\boldsymbol{x}(n)$ such that

$$\boldsymbol{x}(n+1) = \boldsymbol{\mathcal{A}}\boldsymbol{x}(n) + \boldsymbol{\mathcal{B}}\boldsymbol{u}(n) + \boldsymbol{w}(n), \tag{4.1a}$$

$$\boldsymbol{y}(n) = \boldsymbol{\mathcal{C}}\boldsymbol{x}(n) + \boldsymbol{\mathcal{D}}\boldsymbol{u}(n) + \boldsymbol{v}(n). \tag{4.1b}$$

The coefficients of the system matrices are chosen such that the estimated output $\boldsymbol{y}_e(n)$, obtained by time marching (4.1) with $\boldsymbol{w}(n) = \boldsymbol{v}(n) = 0$, is as close as possible to the measured output $\boldsymbol{y}(n)$ (subject to the white-noise sources $\boldsymbol{w}(n)$ and $\boldsymbol{v}(n)$), knowing the inputs $\boldsymbol{u}(n)$. We stress that the state $\boldsymbol{x}(n)$ does not necessarily have to have a physical interpretation.

System identification consists of three procedural steps (see figure 4). First, the system is excited by known and unknown input signals $\boldsymbol{u}(n)$ and $\boldsymbol{w}(n)$ while the outputs $\boldsymbol{y}(n)$ (corrupted by noise $\boldsymbol{v}(n)$) are recorded. In a second step, a parametrized model is chosen, in our case an LTI system characterized by the system matrices $\boldsymbol{\mathcal{A}}$, $\boldsymbol{\mathcal{B}}$, $\boldsymbol{\mathcal{C}}$ and $\boldsymbol{\mathcal{D}}$, together with an appropriate identification algorithm. A subsample of the full dataset, referred to as the learning dataset, is then processed to determine the system matrices of the model. In a third step, a different part of the data, known as the testing dataset, is used to drive the identified system, and the output $\boldsymbol{y}_e(t)$ produced

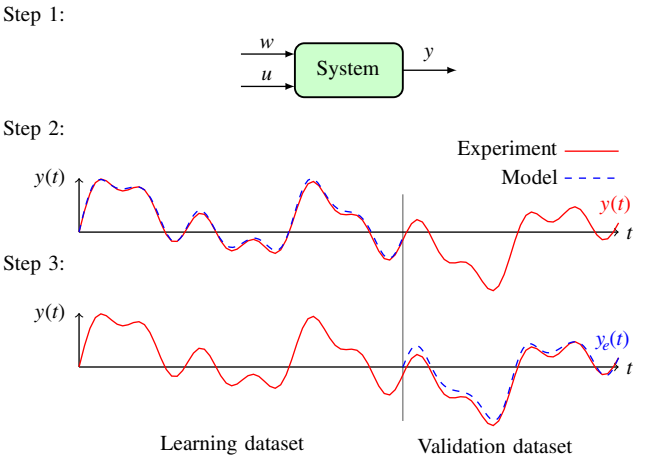


FIGURE 4. (Colour online) Procedural steps of system identification techniques. Step 1: the system is forced with a frequency-rich input signal and data are acquired. The forcing term $w(n)$ driving the system should be either known or replaced by a known proxy measurement $s(n)$. Step 2: after selecting a model structure and appropriate parameters, the model coefficients are then computed by maximizing the fit between the output of the system and the prediction of the model for a part of the available data. Step 3: the model is tested on a dataset different from the one used for learning. If the model does not reproduce the system dynamics with the required accuracy, a different model structure, a different parametrization or even a different experiment should be considered.

by the model is compared to the measured true output $\boldsymbol{y}(t)$; based on this validation test, the model is accepted, adapted or rejected.

The form of the model given in (4.1) makes subspace identification algorithms a convenient choice. Appendix A presents a brief introduction to these techniques; a more comprehensive description is given in Van Overschee & De Moor (1996) and Qin (2006). In this study, the N4SID algorithm (Van Overschee & De Moor 1994) has been used to obtain all the models.

### 4.2. *Outputs as coefficients of velocity snapshots in a POD basis*

We would like to describe the system at each time instant with velocity snapshots $\boldsymbol{u}_{snap}$. The large number of degrees of freedom in these snapshots makes direct application of identification techniques excessively, or prohibitively, expensive. It is thus necessary to reduce the dimensionality of the measured data. In this article, we use the POD modes (Lumley 1967; Sirovich 1987) to form a reduced basis. Note that, contrary to the previous section, the velocity snapshots used to build the POD basis are obtained in the presence of the true, but unknown, noise environment $w(t)$.

We consider a sequence of $m$ velocity snapshots $\{\boldsymbol{V}_{snap}(n)\}_{n=1,\dots,m}$ extracted from the $\Omega_{snap}$ domain and containing the effect of upstream noise $w$. The sequence needs to cover a sufficiently large time range to explore all states of the system. Therefore, even though not mandatory, the time delay between two snapshots can be taken as quite large, so as to obtain nearly uncorrelated successive snapshots. The POD then enables us to compute a ranked orthonormal basis $\{\boldsymbol{\Phi}_i\}_{i=1,\dots,m}$ of flow fields, satisfying $\langle \boldsymbol{\Phi}_i, \boldsymbol{\Phi}_j \rangle = \delta_{ij}, \quad i, j = 1, 2, \dots, m$, which can be expressed most conveniently as a linear combination of these $m$ snapshots. Here, the scalar product $\langle \cdot \rangle$ is associated

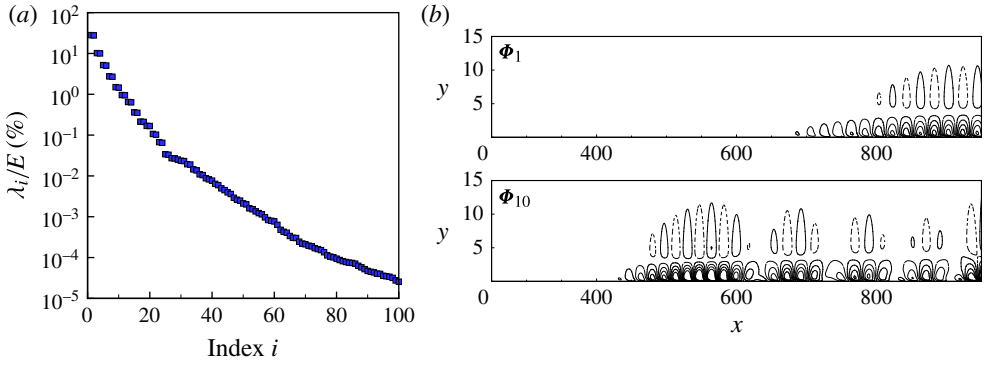


FIGURE 5. (Colour online) (*a*) First 100 POD eigenvalues $\lambda_i$ of the correlation matrix. (*b*) Contours of the streamwise velocity component of the first ($\boldsymbol{\Phi}_1$) and 10th ($\boldsymbol{\Phi}_{10}$) POD modes.

with the energy-based inner product: $\langle \boldsymbol{u}^1_{snap}, \boldsymbol{u}^2_{snap} \rangle = \int_{\Omega_{snap}} (u^1_{snap} u^2_{snap} + v^1_{snap} v^2_{snap})\, \mathrm{d}x\, \mathrm{d}y$. Any velocity field $\boldsymbol{V}$ in $\Omega_{snap}$ can then be projected onto the first $k$ POD modes according to

$$y_i = \langle \boldsymbol{\Phi}_i, \boldsymbol{V} \rangle, \quad i = 1, 2, \ldots, k, \tag{4.2a}$$

$$\boldsymbol{V}' = \sum_{i=1}^{k} \boldsymbol{\Phi}_i y_i, \tag{4.2b}$$

to produce the approximate flow field $\boldsymbol{V}'$. Properties of the POD guarantee that, for all $k$, the error $\|\boldsymbol{V} - \boldsymbol{V}'\|^2 = \langle \boldsymbol{V} - \boldsymbol{V}', \boldsymbol{V} - \boldsymbol{V}' \rangle$ is minimal for the set of $m$ measured snapshots. For the subsequent derivations, we define the reduced state vector given by the $k$ POD coefficients by $\boldsymbol{Y} = [y_1, y_2, \ldots, y_k]^{\mathrm{T}}$ and denote the reduced POD basis by $\boldsymbol{U} = [\boldsymbol{\Phi}_1, \boldsymbol{\Phi}_2, \ldots, \boldsymbol{\Phi}_k]$.

In what follows, snapshots have been obtained with the smaller $\Omega_{snap}$ domain of dimension $(150, 950) \times (0, 40)$. A total of 1500 snapshots sampled each $\Delta t_{pod} = 5$ have been used to obtain the POD basis. From figure 6 a cut-off for the lower frequencies can be established at $f \approx 10^{-3}$, which, considering the total length $T$ of the time data used to compute the POD basis ($T = 1500 \times 5 = 7500$), guarantees that the lowest physical frequencies $f \approx 10^{-3}$ have been explored approximately $7500 \times 10^{-3} \approx 8$ times. Figure 5(*a*) shows the corresponding eigenvalues of the correlation matrix, confirming a steady decay over about three decades in the first 30 modes (95 % of the energy is contained in the first 10 modes). Two selected POD modes, $\boldsymbol{\Phi}_1$ and $\boldsymbol{\Phi}_{10}$, are displayed in figure 5(*b*).

The time-evolving POD coefficients $\boldsymbol{Y}(n)$ constitute the output of the system. In the next section, we will seek a model structure for a dynamic observer that is able to accurately predict $\boldsymbol{Y}(n)$ from the input to the system.

### 4.3. *A dynamic observer obtained by identification techniques*

An approximation $\boldsymbol{Y}_e$ of the temporal evolution of the reduced state vector $\boldsymbol{Y}$ can be obtained by time marching a dynamic observer equation, whose structure is similar to the one given in (3.3), that is,

$$\boldsymbol{Y}_e(n+1) = \widetilde{\boldsymbol{A}}_s \boldsymbol{Y}_e(n) + \widetilde{\boldsymbol{L}} s(n). \tag{4.3}$$

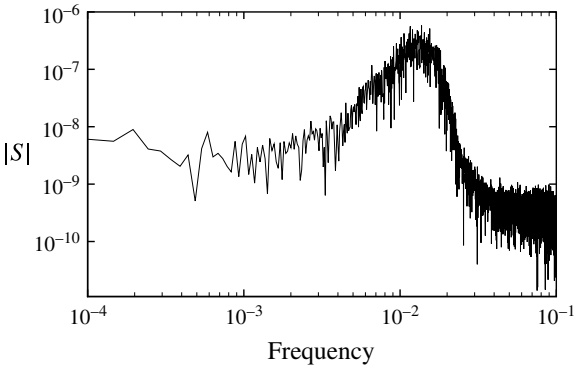


FIGURE 6. Spectrum of the input signal $s(t)$ obtained from the shear-stress sensor placed at $x = 200$.

The quantities $\widetilde{\boldsymbol{A}}_s$, $\widetilde{\boldsymbol{L}}$ and $\widetilde{\boldsymbol{C}}$ will be obtained with system identification techniques that rely solely on knowledge of input–output datasets $\{s(n), \boldsymbol{Y}(n)\}_{n=1,\dots,m}$, rather than by performing a Galerkin projection and solving a Riccati equation. A relation between the general formulation of subspace algorithms defined in § 4.1 and the dynamic observer notation can straightforwardly be defined as $\widetilde{\boldsymbol{A}}_s = \boldsymbol{\mathcal{C}}\boldsymbol{\mathcal{A}}\boldsymbol{\mathcal{C}}^{-1}$ and $\widetilde{\boldsymbol{L}} = \boldsymbol{\mathcal{C}}\boldsymbol{\mathcal{B}}$, assuming that $\boldsymbol{\mathcal{D}} = 0$.

The input $s(n)$ is related to the state $\boldsymbol{Y}_e(n)$ according to

$$s(n) = \widetilde{\boldsymbol{C}}\boldsymbol{Y}_e(n), \tag{4.4}$$

where $\widetilde{\boldsymbol{C}}$ is a measurement matrix, which can be obtained using two different procedures: its exact definition or an identification techniques. In the first case, we combine (2.3) and (4.2) to get

$$\widetilde{\boldsymbol{C}}_{exact,i} = \int_{x_s}^{x_s+\Delta x} \frac{\partial(\boldsymbol{\Phi}_i \cdot \boldsymbol{\tau}_x)}{\partial y}\bigg|_{y=0} \mathrm{d}x, \quad \boldsymbol{\tau}_x = \begin{pmatrix} 1 \\ 0 \end{pmatrix}. \tag{4.5}$$

The evaluation of this expression involves either measuring the POD modes or combining the measurements $\{s(n)\}_{n=1,\dots,m}$ associated with the velocity snapshots $\{\boldsymbol{V}_{snap}(n)\}_{n=1,\dots,m}$, that were used for the construction of the POD basis in § 4.2. In the second case, we use a simple least-squares method applied to a composite time series $\{s(n), \boldsymbol{Y}(n)\}_{n=1,\dots,m}$ of the learning dataset. It is straightforward to show that

$$\widetilde{\boldsymbol{C}} = [s(1) \cdots s(m)][\boldsymbol{Y}(1) \cdots \boldsymbol{Y}(m)]^{\dagger}, \tag{4.6}$$

where $^{\dagger}$ denotes the Moore–Penrose pseudo-inverse.

As shown in § 3.1, the true evolution matrix for $\boldsymbol{Y}$ is not $\widetilde{\boldsymbol{A}}_s$ but $\widetilde{\boldsymbol{A}}_w$. Considering a model structure for $\boldsymbol{Y}$ similar to the one obtained by Galerkin projection in (3.2), we see that the state $\boldsymbol{Y}(n)$ is governed by

$$\boldsymbol{Y}(n+1) = \widetilde{\boldsymbol{A}}_w\boldsymbol{Y}(n) + \widetilde{\boldsymbol{B}}_w w(n), \tag{4.7a}$$

$$s(n) = \widetilde{\boldsymbol{C}}\boldsymbol{Y}(n) + g(n), \tag{4.7b}$$

| | Galerkin projection | System identification |
|---|---|---|
| Reduced-order state | $\boldsymbol{X}(n)$ | $\boldsymbol{Y}(n)$ |
| ROM matrices | $\boldsymbol{A}_w,\ \boldsymbol{B}_w$ | $\widetilde{\boldsymbol{A}}_w,\ \widetilde{\boldsymbol{B}}_w$ |
| Estimated state | $\boldsymbol{X}_e(n)$ | $\boldsymbol{Y}_e(n)$ |
| Observer matrices | $\boldsymbol{A}_s,\ \boldsymbol{L}$ | $\widetilde{\boldsymbol{A}}_s,\ \widetilde{\boldsymbol{L}}$ |
| Measurement matrix | $\boldsymbol{C}$ | $\widetilde{\boldsymbol{C}}_{exact}$ (obtained by definition)<br>$\widetilde{\boldsymbol{C}}$ (obtained by least squares) |

TABLE 1. Notation used for the Galerkin projection and identification based design of a dynamic observer.

where the known input $\widetilde{\boldsymbol{L}}s(n)$ has been replaced by the unknown driving term $\widetilde{\boldsymbol{B}}_w w(n)$. The true evolution matrix $\widetilde{\boldsymbol{A}}_w$ in (4.7) can thus be obtained from the observer matrix $\widetilde{\boldsymbol{A}}_s$ via

$$\widetilde{\boldsymbol{A}}_w = \widetilde{\boldsymbol{A}}_s + \widetilde{\boldsymbol{L}}\widetilde{\boldsymbol{C}}. \tag{4.8}$$

The different notations used for the models obtained with Galerkin projection and identification techniques are summarized in table 1.

### 4.4. *Identification of model coefficients with learning dataset*

We obtain data by performing a linearized DNS of the boundary layer in the presence of unknown noise. We use a sampling interval $\Delta t = 5$ for the velocity snapshots and the shear-stress measurements $s$. This choice of sampling interval can be justified by looking at figure 6, where the frequency spectrum of the input signal $S(f)$ is represented. This figure shows that the frequency content of $s$ is rather low near the Nyquist frequency $f_{Nyquist} = f_s/2 = 0.1$ defined by our sampling interval $\Delta t = 1/f_s$. The datasets to be processed are composed of the input signal from the sensor $s$ and several outputs $y_i$ corresponding to the projection of the snapshots onto the set of POD modes $\{\boldsymbol{\Phi}_i\}$ (figure 7). Using the N4SID algorithm (Van Overschee & De Moor 1994) and the Moore–Penrose pseuso-inverse, the model parameters $\widetilde{\boldsymbol{A}}_s$, $\widetilde{\boldsymbol{L}}$ and $\widetilde{\boldsymbol{C}}$ are then determined by fitting the model output to the true measured output, as the model is forced by the recorded input. A ROM has been determined with $k = 90$ POD modes and a learning dataset of length $N_{snap} = 2000$.

### 4.5. *Assessment of model performance with testing dataset*

The validity of the identified parameters is subsequently confirmed by using a different dataset (referred to as the testing dataset) and by comparing the model output to the true output. As this testing dataset has not been used in the identification of the model, we can assess the predictive capability of the identified model in this manner. The kinetic energy defined as $E(t) = \langle \boldsymbol{u}_{snap}, \boldsymbol{u}_{snap} \rangle \approx \boldsymbol{Y}^*\boldsymbol{Y}$ is an important variable of the system since it represents the global dynamics of the flow. The quality of fit between the energy of the DNS, denoted by $E(t)$, and the value predicted by the model, denoted by $\widetilde{E}(t)$, can be stated as

$$FIT\ \ (\%) = 100\left(1 - \frac{\|E(t) - \widetilde{E}(t)\|}{\|E(t) - \mathrm{mean}(E(t))\|}\right) \tag{4.9}$$

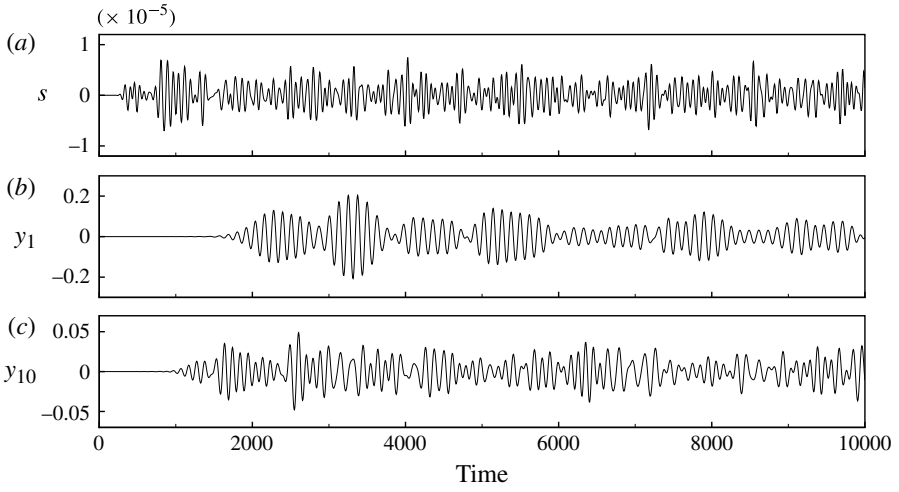


FIGURE 7. Learning dataset: (*a*) the measurement $s$ capturing the influence of external noise and (*b*,*c*) the POD coefficients $y_i$ obtained by projecting the flow field onto the POD modes (*b*) $\boldsymbol{\Phi}_1$ and (*b*) $\boldsymbol{\Phi}_{10}$.

and can be used to quantify the performance of the estimator. Figure 8(*a*) displays the measured input signal $s$ from the wall shear-stress sensor, from which all subsequent flow variables (figure 8*b–e*) can be derived using the identified model. In our case, we show (*b*) the evolution of energy, (*c*,*d*) the first and 10th POD coefficient and (*e*) the output from a friction sensor placed at $x = 600$. After a short transient period, the predicted flow variables closely track their true DNS equivalents, which yields a relative match of $FIT_{ener} = 93.72\,\%$ when evaluated over the time interval $t \in [4000,\ 10\,000]$. The length of the transient period, estimated as $T_{trans} \approx 2000$, can be directly linked to the convective time of the disturbances. As previously mentioned, Tollmien–Schlichting waves are convected with a group velocity equal to $v_g = 0.375$. This convective velocity defines the characteristic time $T_{conv}$ necessary for the wavepacket to cover the distance between the sensor $s$ and the downstream edge of the domain $\Omega_{snap}$. This time ($T_{conv} \approx 2000$) accurately predicts the duration of transient effects $T_{trans}$. This match between the time the estimator needs to propagate information and the time the system needs to convect a wavepacket confirms that the input–output behaviour of the system is well captured by the model. From the POD coefficients in $\boldsymbol{Y}_e$, the full flow field can be reconstructed from the basis $\boldsymbol{U}$. Two examples of this reconstruction, visualized by the streamwise velocity component, are shown in figure 9 and compared to the equivalent full DNS simulation. The first instant at $t = 3000$ has been taken during the transient phase and shows a promising but incomplete match over the entire flow domain; a second instant at $t = 4000$ displays an excellent agreement between the flow structure recovered from $s(t)$ via the identified model and the full DNS solution.

### 4.6. *Influence of some model parameters on performance*

System identification techniques usually contain numerous model parameters, which have to be determined with care in order to obtain a representative and robust model of the underlying physical process. Subspace identification methods are particularly

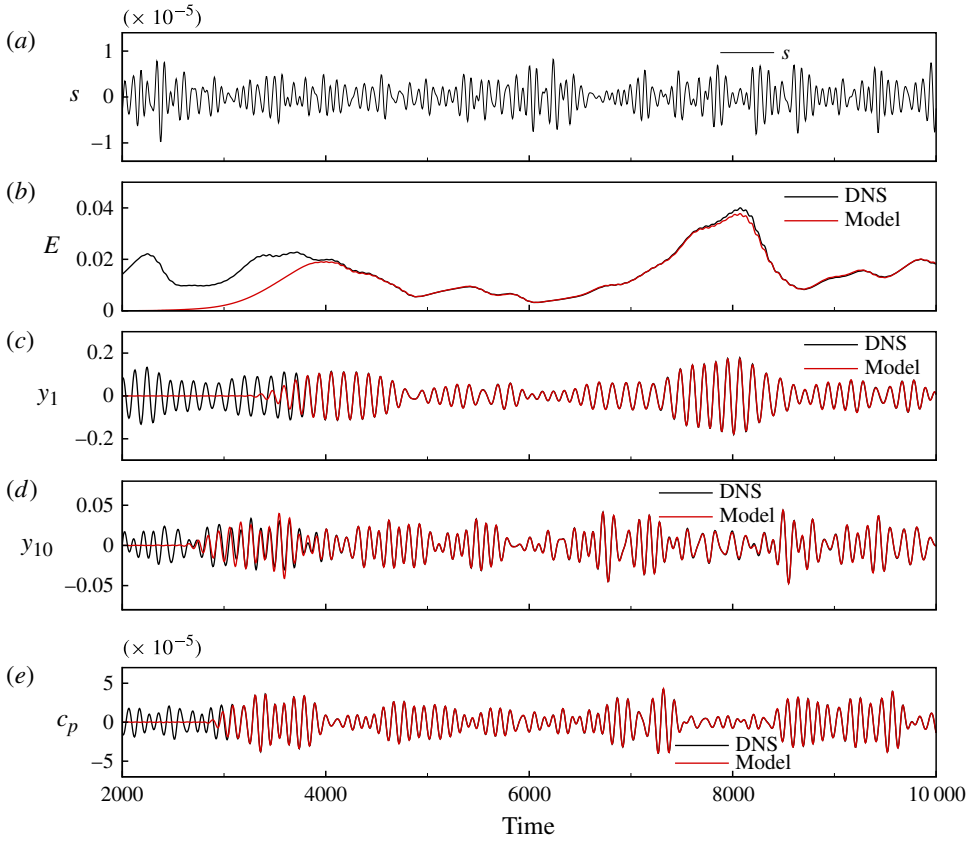


FIGURE 8. (Colour online) Validation dataset: performance of the system identified model, initialized by $\boldsymbol{Y} = 0$ at $t = 2000$. (*a*) The input data from the wall shear-stress sensor $s$; the remaining flow variables are recovered solely from this measurement signal using the identified model. (*b–e*) Comparison between the DNS (black) and the model prediction (grey; red online) for four variables from the testing dataset: (*b*) the energy of the system, (*c*,*d*) the POD coefficients $y_i$ for the first and 10th modes, respectively, and (*e*) a friction sensor $c_p$ placed at $x = 600$.

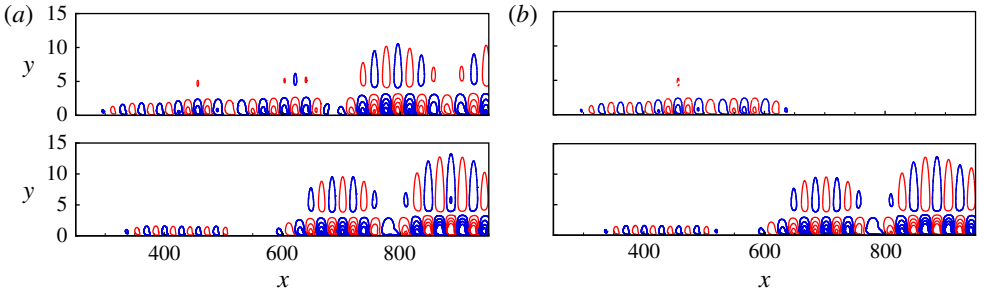


FIGURE 9. (Colour online) Snapshots of the streamwise disturbance velocity component obtained (*a*) from the DNS and (*b*) recovered from $s(n)$ via the model for $t = 3000$ (top) and $t = 4000$ (bottom). See supplementary movie 1 available at http://dx.doi.org/10.1017/jfm.2012.553.

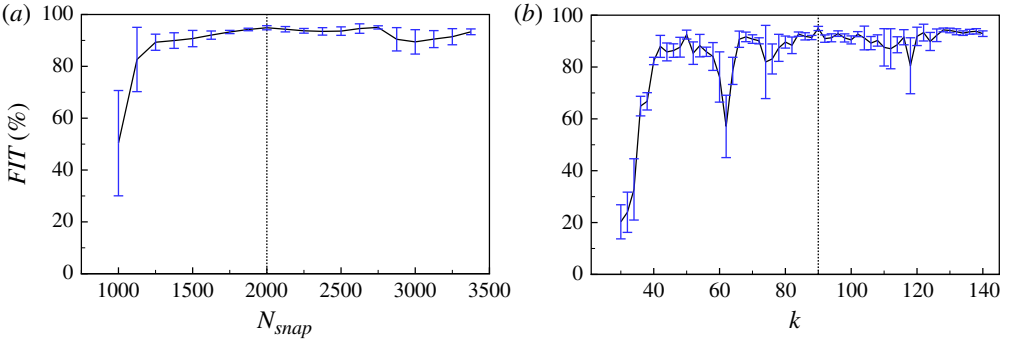


FIGURE 10. (Colour online) Influence of the model parameters on the quality of the identification. Mean (black) and standard deviation (bars; blue online) of the validation fit computed from samples of 10 models obtained from different learning datasets. Influence of (*a*) the length of the learning dataset $N_{snap}$ (for a fixed number of POD modes $N_{pod} = 90$) and (*b*) the number of POD modes $k$ (for a fixed number of snapshots $N_{snap} = 2000$).

advantageous in this respect, when compared to parametrized models (see Hervé *et al.* 2012), owing to the relative simplicity of their parametrization; in fact, the size of the state-space model is the only user-defined parameter for subspace techniques.

In this section, we study the influence of the state-space size $k$ (in other words, the number of POD modes), as well as the number of snapshots $N_{snap}$ contained in the learning dataset, on the quality of our identified ROM. Figure 10 represents the statistical mean and standard deviation of the fit between the validation dataset and the predictions of different models. Both graphs have been obtained by computing, for each point on the curves, 10 models obtained from distinct sections of a long learning dataset. The total length of the learning dataset is $N_{snap} = 8000$ (40 000 time units) and the different learning sections $i$ begin at different time instants, $t^{init}_{i=0,\dots,9} = 2500 + 500i$. Figure 10(*a*) shows, for a fixed number of POD modes ($k = 90$), the influence of the number of snapshots $N_{snap}$: we observe that a minimum number of snapshots are necessary to obtain an accurate model. This observation is common in identification techniques, since the algorithm requires sufficiently long time sequences from the dynamical system to arrive at statistically converged data. In our case, the identification procedure requires about $1500 \times 5 = 7500$ characteristic time units to obtain satisfactory results (signal components of the lowest system frequency $f = 10^{-3}$ have been explored $\sim$8 times).

The influence of the number of POD modes $k$ on the model quality (fit) observed in figure 10(*b*) is far less trivial. For a fixed number of snapshots $N_{snap} = 2000$, a minimum number of $k = 40$–$50$ POD modes are required to obtain a good performance of the dynamic observer: this is related to the concept of observability of the POD basis.

Intuitively, a necessary condition for an observable system requires that the input $s(n)$ and the state $\boldsymbol{Y}(n)$ are well correlated or, in other words, that the measurement $s(n)$ must be accurately representable by the POD coefficients according to $s(n) \approx \widetilde{\boldsymbol{C}}\boldsymbol{Y}(n)$. Figure 11 shows the relative error between the measurement $s(n)$ given by the sensor in the DNS simulation and the measurement $s = \widetilde{\boldsymbol{C}}\boldsymbol{Y}$, with $\boldsymbol{Y}$ obtained by projection of the velocity snapshots onto the POD modes. The solid and dashed lines respectively represent the relative error for the case where $\widetilde{\boldsymbol{C}}$ is obtained by

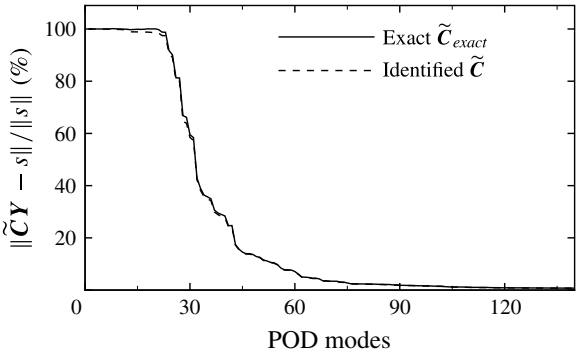


FIGURE 11. Relative error between the signal $s(t)$ obtained by DNS and the signal given by $\widetilde{\boldsymbol{C}}_{exact}\boldsymbol{Y}(t)$ (exact definition) and $\widetilde{\boldsymbol{C}}\boldsymbol{Y}(t)$ (estimated by least squares) for different numbers of POD modes. Here, $\|\cdot\|$ indicates the 2-norm on the vertical axis.

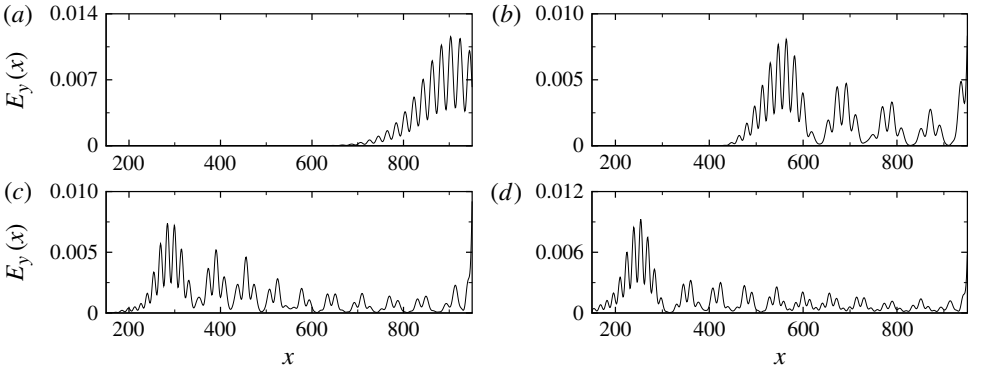


FIGURE 12. Local kinetic energy $E_y(x) = \int_0^\infty (u^2 + v^2)\,\mathrm{d}y$ for four POD modes: (*a*) $\boldsymbol{\Phi}_1$, (*b*) $\boldsymbol{\Phi}_{10}$, (*c*) $\boldsymbol{\Phi}_{22}$ and (*d*) $\boldsymbol{\Phi}_{24}$. The estimation sensor is located at $x_s = 200$.

measuring the POD modes (4.5) and by the pseudo-inverse (4.6). The two curves show a similar behaviour, reflecting the fact that, after a minimum number of POD modes are taken into account, the POD basis accurately captures the temporal behaviour of the measurement signal $s(n)$. The relatively high degree of the system ($N_{pod} = k = 90$) is related to the inherent lack of observability of the POD basis. POD maximizes the energy captured by a few orthogonal modes and, as is the case for the boundary layers (and, more generally, flow amplifiers), the most energetic structures are commonly localized downstream in the domain of interest. Consequently, the first POD modes do not show much spatial support in the upstream part of the domain, and higher modes are necessary to represent the full dynamics of $s(n)$. Figure 12 demonstrates this tendency, showing that the energy content of the modes at the location of the estimation sensor is nearly zero up to the 22nd POD mode.

## 5. Comparison of model obtained by system identification with other techniques

In this section, we compare the performance of our identified dynamic observer to that of a more common Galerkin-based observer (§ 5.1) and to that of an LSE-based observer (§ 5.2).

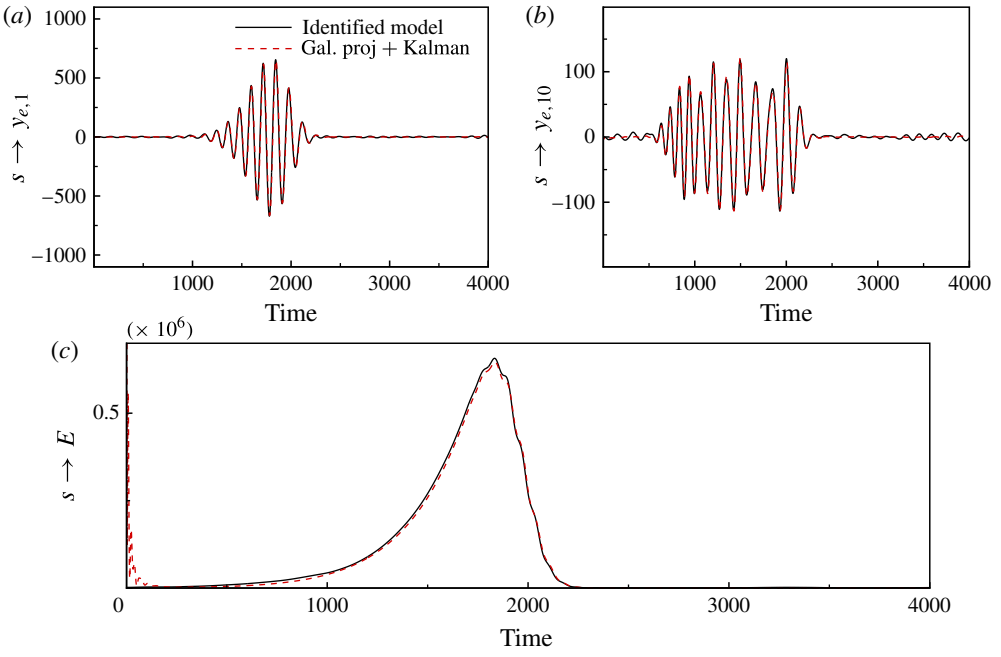


FIGURE 13. (Colour online) Galerkin-based ROM versus estimated model impulse responses: (*a*) from $s$ to $y_{e,1}$, (*b*) from $s$ to $y_{e,10}$ and (*c*) from $s$ to the perturbation energy $E = \boldsymbol{Y}_e^* \boldsymbol{Y}_e$.

### 5.1. *Comparison with model obtained by Galerkin projection*

The identification-based dynamic observer presented in this article is similar to the one obtained by Galerkin projection. However, the identification process will introduce a bias in the obtained model; this bias will be analysed below. In figure 13, we compare the performances of the dynamic observer established in (3.3) by Galerkin projection and the one obtained in (4.3) by identification methods. Even though the temporal evolution of the POD coefficients is quite similar in both models, a slight overestimation in energy is observed in the identified system. The temporal evolution of the POD coefficients furthermore shows small oscillations in the signal of the identified model (noticeable for sufficiently small signal amplitudes; see $3000 < t < 4000$ in figure 13*a*,*b*). This oscillatory effect often appears in identified models and stems from an inadequate representation of some frequencies. It is important, however, to keep in mind that both models are associated with slightly different bases, but a fair comparison has to be performed on a common basis. To this end, we have chosen to project the estimated state $\boldsymbol{X}_e$ onto the POD basis $\boldsymbol{U}$ used to obtain the identified model.

### 5.2. *Comparison with model obtained by LSE*

LSE postulates a static linear relationship between a set of input signals (measurements from sensors) and a set of output variables of the flow. The LSE estimator can be formulated as

$$\boldsymbol{Y}_e(n) = \widetilde{\boldsymbol{R}}\boldsymbol{S}(n), \tag{5.1}$$

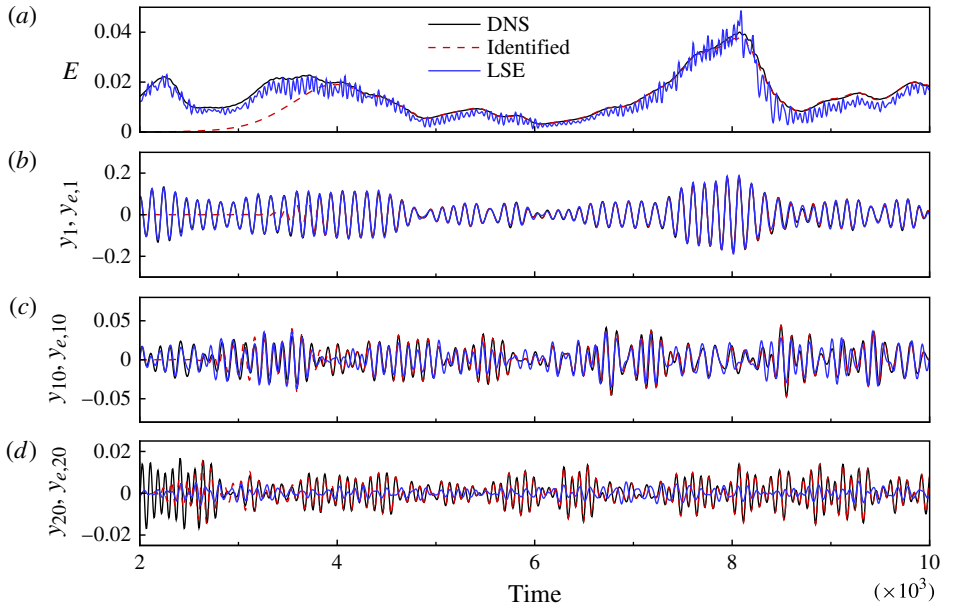


FIGURE 14. (Colour online) Performance of LSE compared to the dynamic observer. The input data used by the LSE model come from 10 equispaced shear-stress sensors between $x = 500$ and $x = 950$, while the dynamic observer uses a single sensor located at $x_s = 200$. (*a–d*) Comparison between the linearized DNS (black full curve), the identified dynamic observer prediction (grey dashed curve; red online) and the LSE model (grey full curve; blue online) for three variables from the testing dataset: (*a*) the energy of the system and (*b–d*) the POD coefficients $y_i$ for the first, 10th and 20th mode, respectively.

where $\boldsymbol{Y}_e(n) \in \mathbb{R}^k$ and $\boldsymbol{S}(n) \in \mathbb{R}^m$ are vectors containing, respectively, the $k$ estimated output variables by LSE at time $n$ and the measurements from $m$ sensors at time $n$, and $\widetilde{\boldsymbol{R}}$ is a matrix obtained by minimizing the mean-squared error between the true output and the one predicted by the model, in other words, $\|\boldsymbol{Y} - \boldsymbol{Y}_e\|^2$.

In our numerical experiments, a linear estimator has been computed based on input from 10 shear-stress sensors (equispaced between $x = 500$ and $x = 950$) and 20 POD modes representing the flow state. Figure 14 shows a comparison of DNS results with results obtained from applying either LSE or a dynamic observer. It appears that, in the case of LSE, a great many more sensors are required to obtain a model of similar quality (performance) than the one provided by the dynamic observer. This observation corroborates the need of the estimator to correctly identify the wavelengths of the Tollmien–Schlichting waves – a requirement that can be met with very closely spaced sensors. By comparing different POD coefficients, this point can be further substantiated. For instance, in figure 14, the first POD coefficient $y_1$ (corresponding to a structure with large wavelengths) is well represented by the model, while the 10th and 20th POD coefficients ($y_{10}$ and $y_{20}$), associated with far shorter wavelengths, deviate more noticeably from the DNS results. Moreover, the energy predicted by the LSE model appears rather noisy compared to the DNS. This feature arises, again, from the poor representation of the shorter wavelengths of the flow, but it also stems from the inherent lack of accuracy of first-order truncated stochastic models. This second source of inaccuracies can be alleviated

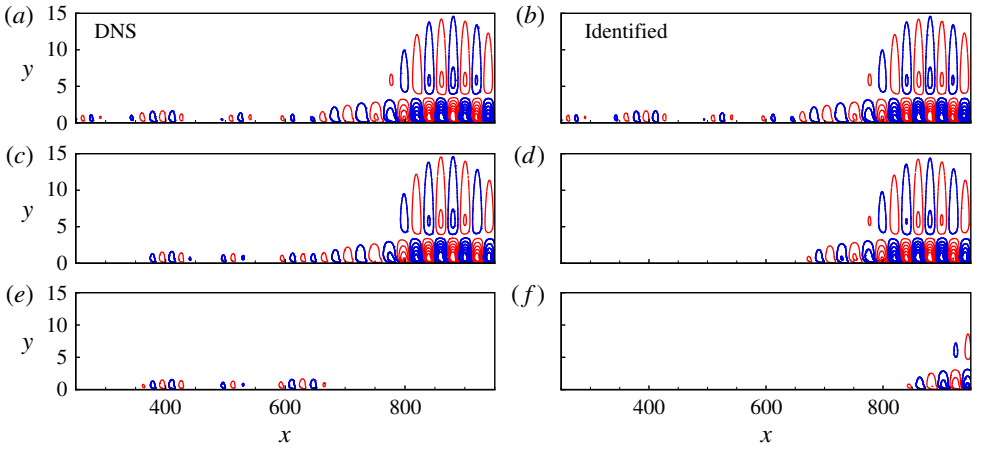


FIGURE 15. (Colour online) Snapshots of the streamwise disturbance velocity at $t = 8000$ ($a$) obtained from linearized DNS, ($b$) recovered from a single sensor via the identified dynamic observer, and ($c$–$f$) recovered from shear-stress sensors via an LSE model: ($c$) from 17 sensors equispaced between $x = 150$ and $x = 950$, ($d$) from 10 sensors equispaced between $x = 500$ and $x = 950$, ($e$) from 10 sensors sensors equispaced between $x = 150$ and $x = 600$ and ($f$) from two sensors placed at $x = 150$ and $x = 950$.

by considering higher-order terms, while adding closer-spaced sensors will achieve a better representation of the poorly estimated wavelengths. It is also important to notice that the linear stochastic estimator does not contain a transient phase, as the dynamic observer does. Furthermore, it needs fewer POD modes: the dynamic observer requires a large number of POD modes to fulfill the observability condition discussed in § 4.6, whereas the linear stochastic estimator is not subjected to this constraint. It has been verified that including more than 20 POD modes does not further improve the performance of the LSE model.

Figure 15 represents snapshots of the streamwise disturbance velocity at a given instant ($t = 8000$) for six different cases. The first two snapshots represent results from the DNS and from a reconstruction by the identified dynamic observer based on a single sensor located at $x_s = 200$, respectively. The last four snapshots are obtained via LSE using different numbers of sensors placed at different positions. In the first of the LSE cases (figure 15$c$), 17 equispaced sensors, located between $x = 150$ and $x = 950$, are considered. A satisfactory prediction of the velocity field is obtained with this configuration, even though the structures far upstream are not as well represented when compared to the dynamic observer. In figure 15($d$,$e$) 10 sensors have been placed equidistantly, in one case, between $x = 500$ and $x = 950$ and, in a second case, between $x = 150$ and $x = 600$. When the 10 sensors are concentrated in the downstream part of the domain, upstream information is lost, and vice versa for an upstream placement of the sensors. Finally, figure 15($f$) uses only two sensors (at $x = 200$ and $x = 950$): this time, LSE fails to recover any relevant information about the flow structures. These results underline the fact that LSE requires spatial support of the input information (sensors) over the whole domain due to the strong convection, while the dynamic observer only needs information from a localized input signal. In summary, the above numerical experiments show that a dynamic observer model is preferable over a linear stochastic estimator (LSE) model in providing an accurate approximation of the flow field from localized and sparse measurements.

## 6. Application of optimal control

The successful recovery of full-state information from single wall shear-stress measurements by a dynamic observer enables the design of a variety of effective control schemes, which we demonstrate next. For this purpose, a control signal $u$ is placed at $(x_u, y_u) = (250, 1)$ (downstream of the sensor $s$), which constitutes a feedforward control configuration. The governing equations (3.3) of the dynamic observer are modified to reflect this addition. We have

$$\boldsymbol{Y}_e(n+1) = \widetilde{\boldsymbol{A}}_s \boldsymbol{Y}_e(n) + \widetilde{\boldsymbol{L}} s(n) + \widetilde{\boldsymbol{B}}_u u(n). \tag{6.1}$$

Following Hervé *et al.* (2012), the system is excited with a frequency-rich signal $u$ in order to identify the new term $\widetilde{\boldsymbol{B}}_u$. The unknown system matrices $\widetilde{\boldsymbol{A}}_s$, $\widetilde{\boldsymbol{L}}$ and $\widetilde{\boldsymbol{B}}_u$ may then be determined in a similar way as described in § 4. From there, the true linear system matrix $\widetilde{\boldsymbol{A}}_w$ that governs the perturbation dynamics ((4.7) with added control term) can be extracted following (4.8). This matrix is then used for the design of a linear–quadratic regulator (LQR) optimal controller $u(n) = \boldsymbol{K}\boldsymbol{Y}(n)$, which minimizes the cost functional $\sum_{n=0}^{\infty} \boldsymbol{Y}(n)^* \boldsymbol{Q} \boldsymbol{Y}(n) + \ell^2 |u(n)|^2$, where $\boldsymbol{Q}$ is a positive definite weight matrix and $\ell$ is a user-specified parameter to balance disturbance energy and exerted control energy. Following a standard procedure (see Burl 1999), the control gain $\boldsymbol{K}$ can be obtained by solving a Riccati equation involving $\widetilde{\boldsymbol{A}}_w$, $\widetilde{\boldsymbol{B}}_u$, $\boldsymbol{Q}$ and $\ell$.

Two different control objectives $\boldsymbol{Q}$ have been considered: (i) the suppression of the energy $E(t)$ inside the velocity window ($\boldsymbol{Q} = \boldsymbol{I}$) and (ii) the control of the signal variance recorded by the downstream friction sensor $c_p$ ($\boldsymbol{Q} = \widetilde{\boldsymbol{C}}_p^* \widetilde{\boldsymbol{C}}_p$, with $\widetilde{\boldsymbol{C}}_p$ the measurement vector associated with $c_p$ and obtained with the least-squares technique introduced in § 4.3 to obtain $\widetilde{\boldsymbol{C}}_s$). We use a model that comprises 50 modes computed on a shorter domain ($\Omega_{snap} = (200, 700) \times (0, 40)$). In the controlled simulation, the measurement $s$ is used to reconstruct the full perturbation field $\boldsymbol{Y}_e$ based on the identified model, and the control law is obtained by applying the control gain $\boldsymbol{K}$ to this state. Results are shown in figure 16 together with the control signal $u(t)$ and the friction-sensor signal $s$. In both cases, a substantial reduction in the respective objectives can be accomplished. The energy $E(t)$ has been reduced by nearly two orders of magnitude (a reduction of 96.81 % in the mean perturbation energy), while the root-mean-square (r.m.s.) value of the friction-sensor signal has been lowered by $\sim$88.01 %.

## 7. Summary and conclusions

A dynamic observer recovering full-state information from single wall shear-stress measurements has been designed that relies on a POD basis (from measured snapshots) and system identification techniques. For noise-amplifier flows, it successfully reproduces the perturbation dynamics (velocity fields) throughout the full sampling domain and furnishes information about the flow that can subsequently be used by itself, for flow diagnostics or, in a second step, for LQR-control design.

Within the limits of linear perturbation dynamics, the design process for the dynamic observer extracts the system matrix from a sequence of snapshots; this system matrix describes a globally stable flow configuration that is sustained by selectively amplified random perturbations from the noise environment. The proposed method thus successfully separates the intrinsic stable perturbation dynamics from the external noise excitation, which previously could only be quantified in its entirety.

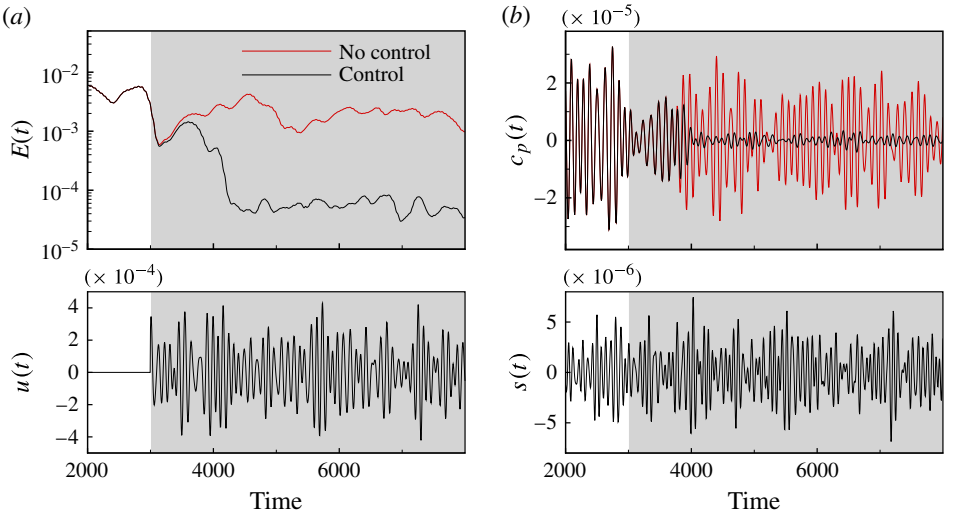


FIGURE 16. (Colour online) Results of the LQR-control design based on the dynamic observer. (*a*) Temporal evolution of the perturbation energy $E(t)$ for the uncontrolled simulation (grey; red online) and the controlled simulation targeting the energy (black), together with the control signal $u(t)$ obtained in the case of the energy objective (see supplementary movie 2). (*b*) Time signal of the friction sensor $c_p(t)$ placed at $(x_{c_p}, y_{c_p}) = (600, 0)$ for the uncontrolled (grey; red online) and controlled simulation targeting the sensor signal $c_p$ (black), together with the sensor signal $s$, which is the same in all simulations discussed in this figure.

A wide variety of flow analyses is possible once the system matrix has been extracted. In the present case, we chose to design a closed-loop control scheme, which, owing to the known system matrix, could now be accomplished using full-state information control (LQR) algorithms. As a consequence, a significant reduction of the perturbation energy or sensor signal r.m.s. values could be achieved. Even though system identification could have been used to determine a direct input-to-output control law targeting the variance of a downstream wall sensor (Hervé *et al.* 2012), the retrieval of full-state information gives a far more physical and structural view of dynamic processes.

The input data for the design procedure of the dynamic observer are readily available in experiments, and an application of a dynamic observer in a suitable experiment is currently planned and will be explored in a future effort. However, difficulties not accounted for in the present paper are expected to arise in an experimental situation: noise corrupting the PIV and friction measurements, the presence of non-localized external forcing or the presence of nonlinearities are some examples. These challenges will be addressed in a forthcoming study.

**Acknowledgements**

The authors would like to thank J. C. Robinet and A. Hervé for fruitful conversations, as well as J. C. Loiseau for his support with Nek-5000.

**Supplementary movies**

Supplementary movies are available at http://dx.doi.org/10.1017/jfm.2014.553.

## Appendix A. Subspace identification algorithms

Subspace identification algorithms consider the state-space formulation of a stochastic linear system. Such a system can be written in the process form

$$\boldsymbol{x}(n+1) = \boldsymbol{\mathcal{A}}\boldsymbol{x}(n) + \boldsymbol{\mathcal{B}}\boldsymbol{u}(n) + \boldsymbol{w}(n), \tag{A 1a}$$

$$\boldsymbol{y}(n) = \boldsymbol{\mathcal{C}}\boldsymbol{x}(n) + \boldsymbol{\mathcal{D}}\boldsymbol{u}(n) + \boldsymbol{v}(n), \tag{A 1b}$$

where $\boldsymbol{y}(n) \in \mathbb{R}^{n_y}$, $\boldsymbol{x}(n) \in \mathbb{R}^{n}$, $\boldsymbol{u}(n) \in \mathbb{R}^{n_u}$, $\boldsymbol{w}(n) \in \mathbb{R}^{n}$, $\boldsymbol{v}(n) \in \mathbb{R}^{n_y}$ are the system output, state, input, state noise and output measurement noise, respectively. The matrices $\boldsymbol{\mathcal{A}}$, $\boldsymbol{\mathcal{B}}$, $\boldsymbol{\mathcal{C}}$ and $\boldsymbol{\mathcal{D}}$ are system matrices of appropriate dimensions. The noise covariances of the system are defined as

$$\mathcal{E}\left\{ \begin{pmatrix} w_j \\ v_j \end{pmatrix} \begin{pmatrix} w_i \\ v_i \end{pmatrix}^{\mathrm{T}} \right\} = \begin{pmatrix} \boldsymbol{\mathcal{Q}} & \boldsymbol{\mathcal{S}} \\ \boldsymbol{\mathcal{S}}^{\mathrm{T}} & \boldsymbol{\mathcal{R}} \end{pmatrix} \delta_{ij}, \tag{A 2}$$

where $\mathcal{E}\{x\}$ stands for the expected-value operator.

The general problem of subspace identification consists of obtaining the system matrices $\boldsymbol{\mathcal{A}}$, $\boldsymbol{\mathcal{B}}$, $\boldsymbol{\mathcal{C}}$ and $\boldsymbol{\mathcal{D}}$, as well as the covariance matrices $\boldsymbol{\mathcal{Q}}$, $\boldsymbol{\mathcal{S}}$ and $\boldsymbol{\mathcal{R}}$, from observing a set of input–output measurements.

### A.1. *Reformulation of the state-space system*

The state-space system (A 1) can be rearranged into two equivalent formulations that emphasize either prediction or estimation (Qin 2006). Considering either formulation, the one-step linear equations can be written as a multi-step matrix-based expression that will form the foundation of subspace system identification techniques.

Assuming that the system is observable, a Kalman filter can be designed to estimate the state variable. We have

$$\hat{\boldsymbol{x}}(n+1) = \boldsymbol{\mathcal{A}}\hat{\boldsymbol{x}}(n) + \boldsymbol{\mathcal{B}}\boldsymbol{u}(n) + \boldsymbol{\mathcal{L}}[\boldsymbol{y}(n) - \boldsymbol{\mathcal{C}}\hat{\boldsymbol{x}}(n) - \boldsymbol{\mathcal{D}}\boldsymbol{u}(n)], \tag{A 3}$$

which (omitting the 'hats') leads to the innovation form

$$\boldsymbol{x}(n+1) = \boldsymbol{\mathcal{A}}\boldsymbol{x}(n) + \boldsymbol{\mathcal{B}}\boldsymbol{u}(n) + \boldsymbol{\mathcal{L}}\boldsymbol{e}(n), \tag{A 4a}$$

$$\boldsymbol{y}(n) = \boldsymbol{\mathcal{C}}\boldsymbol{x}(n) + \boldsymbol{\mathcal{D}}\boldsymbol{u}(n) + \boldsymbol{e}(n), \tag{A 4b}$$

where $\boldsymbol{\mathcal{L}}$ is the Kalman gain (which can be obtained from a Riccati equation) and $\boldsymbol{e}(n) = \boldsymbol{y}(n) - \boldsymbol{\mathcal{C}}\hat{\boldsymbol{x}}(n) - \boldsymbol{\mathcal{D}}\boldsymbol{u}(n)$ is the measurement error.

A third equivalent representation, the predictor form, can be written as

$$\boldsymbol{x}(n+1) = \boldsymbol{\mathcal{A}}_e\boldsymbol{x}(n) + \boldsymbol{\mathcal{B}}_e\boldsymbol{z}(n), \tag{A 5a}$$

$$\boldsymbol{y}(n) = \boldsymbol{\mathcal{C}}\boldsymbol{x}(n) + \boldsymbol{\mathcal{D}}\boldsymbol{u}(n) + \boldsymbol{e}(k), \tag{A 5b}$$

where $\boldsymbol{z}(n) = [\boldsymbol{u}^{\mathrm{T}}(n), \boldsymbol{y}^{\mathrm{T}}(n)]^{\mathrm{T}}$, $\boldsymbol{\mathcal{A}}_e = \boldsymbol{\mathcal{A}} - \boldsymbol{\mathcal{L}}\boldsymbol{\mathcal{C}}$ and $\boldsymbol{\mathcal{B}}_e = [\boldsymbol{\mathcal{B}} - \boldsymbol{\mathcal{L}}\boldsymbol{\mathcal{D}}, \boldsymbol{\mathcal{L}}]$. It should be stressed again that the three model forms can represent the input and output data $(\boldsymbol{u}(n), \boldsymbol{y}(n))$ exactly. We thus have the choice of using any of these models according to convenience.

As a next step, the above one-step vector-based linear difference equations are recast into multi-step matrix-based expressions. We first define an extended state sequence $\boldsymbol{X}(n) = (\boldsymbol{x}(n), \ \boldsymbol{x}(n+1), \ \ldots, \ \boldsymbol{x}(n+N-1))$, which contains $N$ columns describing

the state at $N$ consecutive time steps. By iterating $p$ times the predictor form (A 5), it is straightforward to derive the extended equation

$$\boldsymbol{X}(n) = \mathcal{L}_p \boldsymbol{Z}_p + \mathcal{A}_e^p X(n-p), \tag{A 6}$$

where

$$\mathcal{L}_p = \left(\mathcal{B}_e, \quad \mathcal{A}_e\mathcal{B}_e, \quad \ldots, \quad \mathcal{A}_e^{p-1}\mathcal{B}_e\right), \tag{A 7a}$$

$$\boldsymbol{Z}_p = \begin{pmatrix} z(n-1) & z(n) & \cdots & z(n+N-2) \\ z(n-2) & z(n-1) & \cdots & z(n+N-3) \\ \vdots & \vdots & \ddots & \vdots \\ z(n-p) & z(n-p+1) & \cdots & z(n-p+N-1) \end{pmatrix}. \tag{A 7b}$$

Under the assumption that all eigenvalues of the estimator matrix $\mathcal{A}_e$ fall strictly inside the unit circle and in the limit $p \to \infty$, the term $\mathcal{A}_e^p$ can be neglected. This result can be proven valid even for finite $p$ (Van Overschee & De Moor 1994, 1996). Equation (A 6) can then be simplified to

$$\boldsymbol{X}(n) = \mathcal{L}_p \boldsymbol{Z}_p. \tag{A 8}$$

In addition, if a similar recursive iteration technique is applied to the innovation form (A 4) we obtain

$$\boldsymbol{Y}_f = \mathcal{O}_f \boldsymbol{X}(n) + \mathcal{H}_f \boldsymbol{U}_f + \mathcal{G}_f \boldsymbol{E}_f, \tag{A 9}$$

where the subscript $f$ denotes the future horizon. Next, the input, output and innovation data are arranged into Hankel matrices, denoted respectively by $\boldsymbol{U}_f$, $\boldsymbol{Y}_f$ and $\boldsymbol{E}_f$. The structure of these matrices is as follows:

$$\boldsymbol{U}_f = \begin{pmatrix} \boldsymbol{u}(n) & \boldsymbol{u}(n+1) & \cdots & \boldsymbol{u}(n+N-1) \\ \boldsymbol{u}(n+1) & \boldsymbol{u}(n+2) & \cdots & \boldsymbol{u}(n+N) \\ \vdots & \vdots & \ddots & \vdots \\ \boldsymbol{u}(n+f-1) & \boldsymbol{u}(n+f) & \cdots & \boldsymbol{u}(n+f+N-2) \end{pmatrix}, \tag{A 10}$$

and similar for $\boldsymbol{Y}_f$ and $\boldsymbol{E}_f$.

Furthermore, $\mathcal{O}_f$ is the extended observability matrix, and $\mathcal{H}_f$ and $\mathcal{G}_f$ are Toeplitz matrices of the form

$$\mathcal{O}_f = \begin{pmatrix} \mathcal{C} \\ \mathcal{C}\mathcal{A} \\ \vdots \\ \mathcal{C}\mathcal{A}^{f-1} \end{pmatrix}, \tag{A 11a}$$

$$\mathcal{H}_f = \begin{pmatrix} \mathcal{D} & 0 & \cdots & 0 \\ \mathcal{C}\mathcal{B} & \mathcal{D} & \cdots & 0 \\ \vdots & \vdots & \ddots & \vdots \\ \mathcal{C}\mathcal{A}^{f-2}\mathcal{B} & \mathcal{C}\mathcal{A}^{f-3}\mathcal{B} & \cdots & \mathcal{D} \end{pmatrix}, \tag{A 11b}$$

$$\mathcal{G}_f = \begin{pmatrix} \mathcal{I} & 0 & \cdots & 0 \\ \mathcal{C}\mathcal{L} & \mathcal{I} & \cdots & 0 \\ \vdots & \vdots & \ddots & \vdots \\ \mathcal{C}\mathcal{A}^{f-2}\mathcal{L} & \mathcal{C}\mathcal{A}^{f-3}\mathcal{L} & \cdots & \mathcal{I} \end{pmatrix}. \tag{A 11c}$$

Combining (A 8) and (A 9) we obtain

$$\boldsymbol{Y}_f = \boldsymbol{\mathcal{H}}_{fp}\boldsymbol{Z}_p + \boldsymbol{\mathcal{H}}_f\boldsymbol{U}_f + \boldsymbol{\mathcal{G}}_f\boldsymbol{E}_f, \tag{A 12}$$

where $\boldsymbol{\mathcal{H}}_{fp} = \boldsymbol{\mathcal{O}}_f\boldsymbol{\mathcal{L}}_p$ is the product of the process observability matrix and the predictor controllability matrix. Equation (A 12) plays an essential role in subspace identification algorithms.

### A.2. *Extraction of the observability matrix* $\boldsymbol{\mathcal{O}}_f$

The goal of the subsequent steps is to recover the matrix $\boldsymbol{\mathcal{H}}_{fp}\boldsymbol{Z}_p$, and then $\boldsymbol{\mathcal{O}}_f$ from it. First, $\boldsymbol{U}_f$ is eliminated from (A 12) by post-multiplying by the projection onto its orthogonal complement $\boldsymbol{\mathcal{P}}^{\perp}_{U_f} = \boldsymbol{\mathcal{I}} - \boldsymbol{U}_f^{\mathrm{T}}(\boldsymbol{U}_f\boldsymbol{U}_f^{\mathrm{T}})^{-1}\boldsymbol{U}_f$. In addition, if we assume that the innovation sequence $e(n)$ is composed of a stationary white noise completely uncorrelated with the input $u(n)$, we have $\boldsymbol{E}_f\boldsymbol{\mathcal{P}}^{\perp}_{U_f} = \boldsymbol{E}_f$, which yields

$$\boldsymbol{Y}_f\boldsymbol{\mathcal{P}}^{\perp}_{U_f} = \boldsymbol{\mathcal{H}}_{fp}\boldsymbol{Z}_p\boldsymbol{\mathcal{P}}^{\perp}_{U_f} + \boldsymbol{\mathcal{G}}_f\boldsymbol{E}_f. \tag{A 13}$$

It is also known from Kalman filter theory that $\boldsymbol{E}_f$ is uncorrelated with $\boldsymbol{Z}_p$. Consequently, the noise term $\boldsymbol{E}_f$ can be removed by multiplying (from the right) (A 13) by $\boldsymbol{Z}_p^T$, which yields

$$\boldsymbol{Y}_f\boldsymbol{\mathcal{P}}^{\perp}_{U_f}\boldsymbol{Z}_p^T = \boldsymbol{\mathcal{H}}_{fp}\boldsymbol{Z}_p\boldsymbol{\mathcal{P}}^{\perp}_{U_f}\boldsymbol{Z}_p^T \tag{A 14}$$

and

$$\boldsymbol{\mathcal{H}}_{fp}\boldsymbol{Z}_p = \boldsymbol{Y}_f\boldsymbol{\mathcal{P}}^{\perp}_{U_f}\boldsymbol{Z}_p^T(\boldsymbol{\mathcal{P}}^{\perp}_{U_f}\boldsymbol{Z}_p^T)^{-1}. \tag{A 15}$$

Finally, from (A 8) we obtain that $\boldsymbol{\mathcal{H}}_{fp}\boldsymbol{Z}_p = \boldsymbol{\mathcal{O}}_f\boldsymbol{X}(n)$. Assuming that the input $u(n)$ is sufficiently rich in temporal behaviour to excite all the observable dynamics of the system, matrix $\boldsymbol{X}(n)$ is ensured to be full row-ranked. In addition, $\boldsymbol{\mathcal{O}}_f$ has full column-rank under the assumption of full observability. These properties suggest applying a singular value decomposition (SVD): (i) to determine the order of the identified system as the rank of $\boldsymbol{\mathcal{O}}_f\boldsymbol{X}(n)$ and (ii) to isolate $\boldsymbol{\mathcal{O}}_f$. Mathematically, this amounts to

$$\boldsymbol{\mathcal{H}}_{fp}\boldsymbol{Z}_p = \begin{pmatrix}\mathcal{U}_1 & \mathcal{U}_2\end{pmatrix}\begin{pmatrix}\mathcal{S}_1 & 0\\ 0 & \mathcal{S}_2\end{pmatrix}\begin{pmatrix}\mathcal{V}_1^{\mathrm{T}}\\ \mathcal{V}_2^{\mathrm{T}}\end{pmatrix}, \tag{A 16}$$

where the diagonal matrix $\boldsymbol{\mathcal{S}}$ has been partitioned so that $\mathcal{S}_2$ is negligible compared to $\mathcal{S}_1$. The size of $\mathcal{S}_1$ then represents the order of the identified system. Moreover, the extended observability matrix $\boldsymbol{\mathcal{O}}_f$ can be extracted according to

$$\boldsymbol{\mathcal{O}}_f = \mathcal{U}_1\mathcal{S}_1^{\frac{1}{2}}. \tag{A 17}$$

### A.3. *Extraction of the system matrices*

Based on $\boldsymbol{\mathcal{O}}_f$, two different approaches may be adopted to extract the system matrices. The first one, denoted as estimation focus, extracts only the system matrices $\mathcal{A}$, $\mathcal{B}$, $\mathcal{C}$ and $\mathcal{D}$ from the data. On the other hand, if the noise covariances are needed, a more complex algorithm, a simulation focus technique, is called for. In this article, we will briefly introduce the first approach, while a detailed description of the second one can

be found in Van Overschee & De Moor (1994, 1996) or Juillet, Schmid & Huerre (2013).

The first step consists in extracting the matrices $\mathcal{A}$ and $\mathcal{C}$ from $\mathcal{O}_f$. This can be accomplished rather easily by computing the matrix $\mathcal{O}_{f-1}$ as previously done with $\mathcal{O}_f$ and by recalling that, by definition, the two matrices are related by the equation

$$\begin{pmatrix} \mathcal{I} & 0 \\ 0 & \mathcal{O}_{f-1} \end{pmatrix} \begin{pmatrix} \mathcal{C} \\ \mathcal{A} \end{pmatrix} = \mathcal{O}_f, \tag{A 18}$$

which can be solved by least-squares techniques. To determine the remaining matrices $\mathcal{B}$ and $\mathcal{D}$, one uses the fact that the problem is linear in these matrices; a simple least-squares matching to the output data may be used to find the remaining matrices (Van Overschee & De Moor 1996).

## REFERENCES


ADRIAN, R. J. 1979 Conditional eddies in isotropic turbulence. *Phys. Fluids* **22**, 2065–2070.

BAGHERI, S., BRANDT, L. & HENNINGSON, D. S. 2009 Input–output analysis, model reduction and control of the flat-plate boundary layer. *J. Fluid Mech.* **620** (1), 263–298.

BARBAGALLO, A., SIPP, D. & SCHMID, P. J. 2009 Closed-loop control of an open cavity flow using reduced-order models. *J. Fluid Mech.* **641** (1), 1–50.

BERGMANN, M., BRUNEAU, C.-H. & IOLLO, A. 2009 Enablers for robust POD models. *J. Comput. Phys.* **228** (2), 516–538.

BONNET, J.-P., COLE, D. R., DELVILLE, J., GLAUSER, M. N. & UKEILEY, L. S. 1994 Stochastic estimation and proper orthogonal decomposition: complementary techniques for identifying structure. *Exp. Fluids* **17**, 307–314.

BURL, J. B. 1999 *Linear Optimal Control*. Addison-Wesley Longman.

BUTLER, K. M. & FARRELL, B. F. 1992 Three-dimensional optimal perturbations in viscous shear flow. *Phys. Fluids* A*: Fluid Dyn.* **4** (8), 1637–1650.

DERGHAM, G., SIPP, D. & ROBINET, J. C. 2013 Stochastic dynamics and model reduction of amplifier flows: the backward facing step flow. *J. Fluid Mech.* **719**, 406–430.

GUEZENNEC, Y. G. 1989 Stochastic estimation of coherent structures in turbulent boundary layers. *Phys. Fluids* **1**, 1054–1060.

HERVÉ, A., SIPP, D., SCHMID, P. J. & SAMUELIDES, M. 2012 A physics-based approach to flow control using system identification. *J. Fluid Mech.* **702**, 26–58.

HUDY, L. M., NAGUIB, A. & HUMPHREYS, W. M. 2007 Stochastic estimation of a separated flow field using wall-pressure array measurements. *Phys. Fluids* **19**, 024103.

JUILLET, F., SCHMID, P. J. & HUERRE, P. 2013 Control of amplifier flows using subspace identification techniques. *J. Fluid Mech.* **725**, 522–565.

KIM, J. & BEWLEY, T. R. 2007 A linear systems approach to flow control. *Annu. Rev. Fluid Mech.* **39**, 383–417.

LEWIS, J. M., LAKSHMIVARAHAN, S. & DHALL, S. 1989 *Dynamic Data Assimilation: A Least Squares Approach*, vol. 13, Encyclopedia of Mathematics and its Applications. Cambridge University Press.

LJUNG, L. 1999 *System Identification: Theory for the User*. Prentice-Hall PTR.

LUMLEY, J. L. 1967 The structure of inhomogeneous turbulent flows. In *Atmospheric Turbulence and Radio Wave Propagation*, pp. 166–178. Nauka.

MOORE, B. 1981 Principal component analysis in linear systems: controllability, observability, and model reduction. *IEEE Trans. Autom. Control* **26** (1), 17–32.

QIN, S. J. 2006 An overview of subspace identification. *Comput. Chem. Engng* **30** (10), 1502–1513.

ROWLEY, C. W. 2005 Model reduction for fluids, using balanced proper orthogonal decomposition. *Intl J. Bifurcation Chaos* **15** (3), 997–1013.

ROWLEY, C. W. & JUTTIJUDATA, V. 2005 Model-based control and estimation of cavity flow oscillations. In *Proceedings of the 44th IEEE Conference on Decision and Control, 2005 and 2005 European Control Conference (CDC-ECC'05)*, pp. 512–517. IEEE.

SIROVICH, L. 1987 Turbulence and the dynamics of coherent structures. *Q. Appl. Maths* **45**, 561–571.

TAYLOR, J. A. & GLAUSER, M. N. 2004 Towards practical flow sensing and control via POD and LSE based low-dimensional tools. *Trans. ASME: J. Fluids Engng* **126** (3), 337–345.

TINNEY, C. E., COIFFET, F., DELVILLE, J., HALL, A. M., JORDAN, P. & GLAUSER, M. N. 2006 On spectral linear stochastic estimation. *Exp. Fluids* **41**, 763–775.

TU, J. H., GRIFFIN, J., HART, A., ROWLEY, C. W., CATTAFESTA, L. N. III & UKEILEY, L. S. 2013 Integration of non-time-resolved PIV and time-resolved velocity point sensors for dynamic estimation of velocity fields. *Exp. Fluids* **54** (2), 1–20.

VAN OVERSCHEE, P. & DE MOOR, B. 1994 N4SID: subspace algorithms for the identification of combined deterministic–stochastic systems. *Automatica* **30** (1), 75–93.

VAN OVERSCHEE, P. & DE MOOR, B. 1996 *Subspace Identification for Linear Systems*. Kluwer.